Journal Name

ARTICLE

Localized mechanical stimulation of single cells with engineered spatio-temporal profile

Received 00th January 20xx,
Accepted 00th January 20xx

DOI: 10.1039/x0xx00000x

www.rsc.org/

M. Monticelli,*[a] D. S. Jokhun,[b] D. Petti,[a] G. V. Shivashankar[bcd] and R. Bertacco[ae]

In-vivo, cells are frequently exposed to multiple mechanical stimuli arising from the extracellular microenvironment, with deep impact on many biological functions. On the other hand, current methods for mechanobiology do not allow to easily replicate in-vitro the complex spatio-temporal profile of such mechanical signals. Here we introduce a new platform for studying the mechanical coupling between single cells and a dynamic extracellular environment, based on active substrates for cell culture made of Fe-coated polymeric micropillars. Under the action of quasi-static external magnetic fields, each group of pillars produces synchronous mechanical stimuli at different points of the cell membrane, thanks to the highly controllable pillars' deflection. This method allows to exert complex stress fields, resulting in the parallel application of localized forces with tunable intensity and temporal profile. The platform has been validated by studying the cellular response to periodic stimuli in NIH3T3 fibroblasts. We find that low-frequency mechanical stimulation affects the actin cytoskeleton, nuclear morphology, H2B core-histone dynamics and induces MKL transcription-cofactor translocation from nucleus to cytoplasm. The unique capability of the proposed platform to apply stimuli with tunable temporal profile and high parallelism on a cell culture, holds great potential for the investigation of mechanotransduction mechanisms in cells and tissues.

Introduction

In the last two decades, a growing scientific interest has been attracted by the emerging field of *mechanobiology*, which aims at studying the modifications of cell properties, and related transduction mechanisms, occurring when cells sense and respond to mechanical stimuli. Recent works[1,2,3,4] have highlighted how infected and mutated cells exhibit altered mechanical properties and specific mechanically activated biochemical pathways, whose understanding can be crucial for the diagnosis and treatment of several diseases.

In particular, mechanical interactions between extracellular matrix and cells play a fundamental role in regulating behaviors such as migration[5], differentiation[6] and proliferation[7]. In these cellular processes, matrix signals are transduced from the peripheral area to the nucleus, eventually resulting in alterations of gene expression[8]. Various studies aim at investigating the nuclear response to mechanical stimuli applied on the cell membrane, and explore how the cytoskeleton mediates mechanical force transduction from the peripheral area to the nucleus[9,10,11]. However, a precise understanding of these mechanisms is still limited by the inherent difficulties to reproduce in-vitro the stress fields applied to the cell in-vivo. The most common methods for studying mechanotransduction include atomic force microscopy[12], magnetic[13,14,15,16] and optical tweezers[17], micropipette aspiration[18,19], parallel plate compression[20] and induced uniform strain on deformable substrates[21,22]. A few studies have shown that cells and nuclei change shape in response to physical confinement, like that induced by microposts[23,24,25], micropatterned adhesive molecules[26,27] and constrictions in microfluidic channels[28]. Polymeric substrates with active functionalities[29,30] have been proposed, including magnetic microposts[31,32] and arrays of magnetic pillars embedded in an elastomer[33]. Nevertheless, the aforementioned techniques are unable to simultaneously apply localized forces at multiple points of the same cell with tunable spatio-temporal profile. Furthermore, as stimulation is carried out by manipulating localized magnetic field sources, they lack of the parallelism needed to reproduce in-vitro mechanical stimuli from the extracellular matrix on a whole cell culture[34,35].

Here we present a novel platform for mechanobiology: an active substrate for cell culture consisting in an array of groups of PDMS pillars with magnetic heads. Under the action of an external quasi-static magnetic field, all groups of pillars stretch and retract synchronously, thus exerting a sort of local "pinching" on the cell membrane, at the points of adhesion (see Fig. 1a). In the specific case of square groups of *Fe*-coated micropillars, a rotating magnetic field

[a] *Department of Physics, Politecnico di Milano, Milan, Italy. E-mail: marco.monticelli@polimi.it*
[b] *Mechanobiology Institute, National University of Singapore, Singapore.*
[c] *Department of Biological Sciences, National University of Singapore, Singapore.*
[d] *Institute of Molecular Oncology, Italian Foundation for Cancer Research, Milan, Italy.*
[e] *IFN-CNR, c/o Politecnico di Milano, Milan, Italy.*
† Electronic Supplementary Information (ESI) available: [details of any supplementary information available should be included here]. See DOI: 10.1039/x0xx00000x

in the plane of the substrate induces a continuous biaxial deformation of the pillars, up to a maximum deflection of 600 nm for an applied field of 100 mT. This produces a periodic and local cell pinching with a maximum strain of ~5% on the cell membrane. By tuning both the magnitude and direction of the external magnetic field, our platform allows for the real-time control of the intensity and temporal profile of the applied stress field.

The potential of this method has been assessed in experiments aiming at studying the cellular and nuclear response to the periodic pinching produced by magnetic pillars. The prolonged application of local forces on single fibroblast cells, with amplitude of a few tens of nN and frequency of 0.1 Hz, affects the nuclear morphology and deformability, as well as the turnover of H2B core-histone, a protein of the chromatin. Interestingly enough, the dynamics of nuclear response is much slower and uncorrelated to the temporal evolution of the stimuli, thus suggesting that the coupling is not simply elastic but mediated by active cellular mechanisms involving cytoskeleton reorganization and biomolecular processes across the nuclear membrane. This emerges from the observed enhancement in actin dynamics and translocation of *megakaryoblastic acute leukemia factor-1* (MKL) transcription cofactor from the nucleus to the cytoplasm during stimulation.

To the best of our knowledge this is the first example of a study in the field of mechanobiology using a periodic local stimulation at multiple cell adhesion points.

Our results show that the proposed platform holds potential for the in-vitro study of mechanotransduction mechanisms and cellular response to mechanical stimuli with well-defined spatio-temporal behavior, allowing to mimic complex and localized stimuli exerted by a dynamic extracellular microenvironment.

Materials and methods

Magnetic pillars fabrication

The active substrate is made of Polydimethylsiloxane (PDMS) pillars with *Fe* ferromagnetic heads, patterned in arrays of repeated groups of four (see Fig. 1b). Each pillar is 10 µm high and 5 µm wide, with a minimum distance between adjacent pillars of 2 µm, in absence of magnetic field. The distance between neighbouring groups is 6 µm, so as to neglect the magnetic interaction between them. They are fabricated by replica moulding (see the ESI†, Fig. S1) from a *Si* substrate, patterned by photolithography and reactive ion etching. PDMS (mixing ratio= 10 elastomer : 1 curing-agent) is cast on top of the mould and thermally cured at 80 degrees for 3 hours, before the peeling procedure. On top of PDMS a tri-layer of SiO_2 (50 nm) / *Fe* (150 nm) / SiO_2 (50 nm) is deposited by e-beam evaporation (see Fig. 1c). The first SiO_2 layer favours the adhesion of *Fe* on top of PDMS, while the second layer isolates the magnetic material from the biological environment. *Fe* is chosen as ferromagnetic material for pillars actuation due to its reduced toxicity together with a large saturation magnetization (M_S= $1.72 \cdot 10^6$ Am^{-1}).

Micromagnetic simulations and Magnetic force calculation

Simulations to quantify the force between the magnetic pillars are performed using OOMMF (Object Oriented Micro Magnetic Framework)[36]. The micromagnetic configuration of *Fe*-disks (see Fig. 1d) and the related magnetic stray field are calculated using standard parameters for *Fe*: saturation magnetization M_s= $1.72 \cdot 10^6$ $A \cdot m^{-1}$, exchange stiffness A= $2.1 \cdot 10^{11}$ $J \cdot m^{-1}$, damping coefficient τ= 0.01 and null magneto-crystalline anisotropy. This last assumption is supported by the magnetic characterization of the pillars performed by Vibrating sample magnetometetry (see the ESI†, section S2 and Fig. S4), showing that the deposited *Fe* is magnetically isotropic.

A 20x20x20 nm^3 unit cell has been used. Although the exchange length of iron is 2.4 nm, this represents a reasonable compromise ensuring reduced computational times. We have checked that using cubic unit cells with a side length of 5 nm does not introduce major modifications in the simulated stray field.

The magnetic force is calculated from the stray field produced by the adjacent disks, according to the following equation[37]:

$$\mathbf{F}_M = \mu_0 \nabla(\mathbf{m} \bullet \mathbf{H}) = \mu_0 \int_V \nabla(M \bullet \mathbf{H}) dV \quad (1)$$

where **m** is the magnetic moment of *Fe*-disks and **M** the magnetization, considered uniform all over the disk volume, according to micromagnetic simulations (see the ESI†, section S1 and Fig. S3). **H** is the total field (**H= H_d + H_e**), calculated using OOMMF, resulting from the sum of the stray field generated by the adjacent pillars (**H_d**) and the external magnetic field (**H_e**). The integration is performed numerically (with a custom written code in *MATLAB*) over the *Fe*-disk volume (V).

Cell Culture and Plasmid Transfections.

NIH3T3 fibroblasts stably expressing H2B-EGFP were cultured in low-glucose Dulbecco's Modified Eagle Medium (Gibco; LifeTechnologies) supplemented with 10% (vol/vol) FBS (Gibco; Life Technologies) and 1% penicillin-streptomycin (Gibco; Life Technologies) at 37 °C and 5% CO_2 in humid conditions. Cells were transfected with RFP-Lifeact or mcherry-MKL by electroporation (Gibco; Life Technologies), the day before the experiment. Cells were trypsinized (Gibco; Life Technologies) and seeded on micropillars coated with 20 µg/ml of Bovine Serum Albinum (BSA, Sigma Aldrich) and Fibronectin (Gibco; Life Technologies) for 3 h followed by 100 µg/ml of fibronectin for 1 h. Before imaging, the chip was inverted in a petri dish, on two *parafilm* spacers to avoid contact between the cells and the bottom of the dish. A special medium (Gibco; Life Technologies, catalogue number: 18045), not requiring a CO_2-rich atmosphere, was used during the experiments.

Imaging, Magnetic field application and Image Processing.

The dish containing our active substrate with the cells cultured on the pillars was placed under a NikonA1R Confocal microscope with 20x and 40x objectives. The rotating magnetic field is applied via two $Nd_2Fe_{14}B$ permanents magnets, mounted on a rotating 3D-printed support, which was mechanically isolated from both the microscope and the sample stage (see the experimental setup in the ESI†, Fig. S2). The Magnetic field rotation is provided by a stepper motor, regulated by an *Arduino UNO* microcontroller. Acquisition is performed in bright field and confocal mode with different acquisition rates according to the experiments: 0.5 fps for fast dynamics and 3 frames

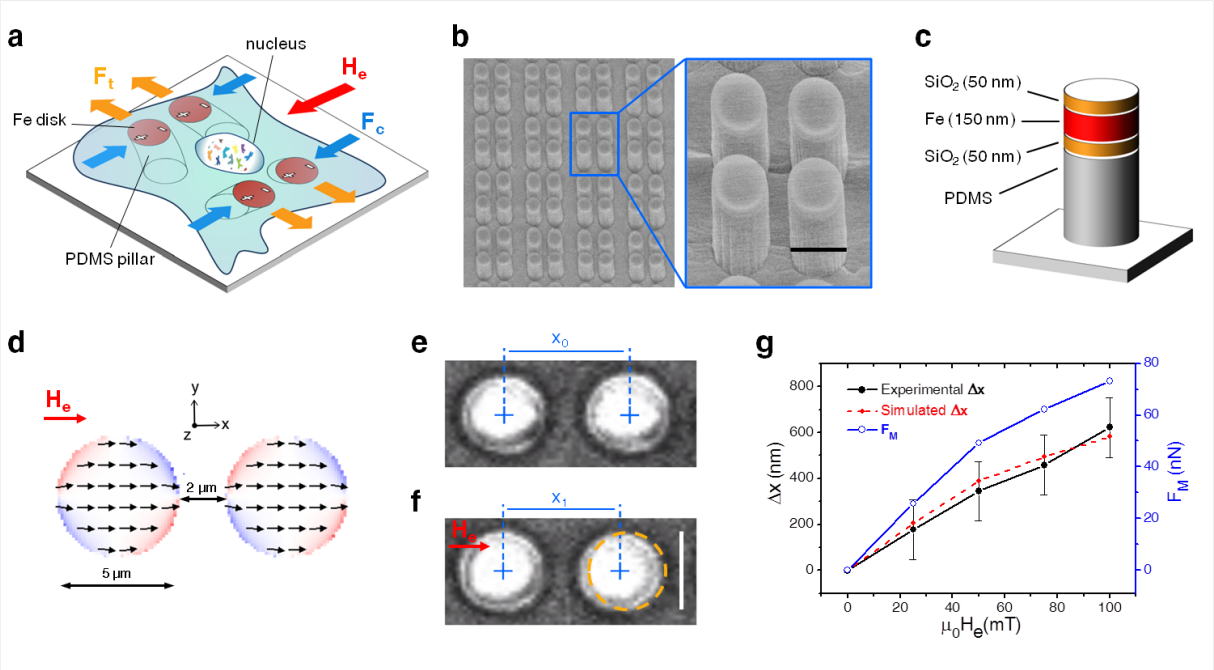

per minute for slow dynamics. The *z*-depth for confocal imaging is ~500 nm. A custom written code in *MATLAB* was used for H2B-EGFP image thresholding, projected nuclear area calculation, geometrical parameters extrapolation (see Fig. 3a-c) and images correlation analysis (see Fig. 5b). *Fluorescence Recovery After Photobleaching* (FRAP, see Fig. 4c,d) and mcherry-MKL intensity analysis (see Fig. 5c,e) were performed with the *ImageJ* software. MKL-intensity images subtraction was performed using *MATLAB* (see Fig. 5d). The pillars deflections (in Fig. 1e,f) were measured with a NIKON-eclipse optical microscope equipped with a 60x immersion objective.

Nuclear Area fluctuations analysis

The effect of mechanical stimuli on the nuclear plasticity and deformability was investigated by extrapolating the nuclear area fluctuations (see Fig. 4a,b). In this procedure[26], the absolute projected nuclear area was first measured by thresholding the average intensity projection of confocal *z*-slices of the H2B-EGFP positive nuclei. This projected area was then plotted as a function of time and fitted with third-order polynomial curves. The residual values were divided by the value of the polynomial at each time point and multiplied by 100 to obtain the percentage nuclear area fluctuations (PNAF). Such PNAFs from n=10 cells and all the time points, were combined to obtain a normal distribution, either from data acquired before and during pinching. Standard deviations of the PNAF distributions before and during pinching (σ_{BP} and σ_{DP}) indicate the amplitude (in percentage) of area fluctuations in the two cases.

FRAP Analysis

To investigate the effect of pinching on H2B core histone dynamics, a *Fluorescence Recovery After Photobleaching* (FRAP) experiment was performed on H2B-EGFP labelled cells (see Fig. 4c,d). First, a circular region (~4 µm in diameter) in the nucleus was photobleached. Then images were acquired at 12 frames per minute during the first 5 minutes, to capture the fast dynamics of the fluorescence recovery, and then at 3 frames per minute for 20 minutes. Using the *ImageJ* software, the fluorescence intensity in the photobleached region is computed at each time frame, before and after photobleaching. A normalized intensity (I_{norm}) is calculated using the following formula:

Fig. 1 Magnetic pillars working principle and characterization. (a) Sketch of the device showing a group of 4 *Fe*-coated pillars with a cell cultured on top. The application of a uniform external magnetic field ($\mathbf{H_e}$) induces adjacent pillars interaction, producing pillars bending and thus applying mechanical stimuli on cells. Compression of adjacent pillars occurs in the field direction, while they are stretched in the perpendicular one. On top of *Fe*-disks, the magnetic charges induced by $\mathbf{H_e}$ are depicted. Blue and orange arrows represent the magnetic force components, compressive ($\mathbf{F_c}$) and tensile ($\mathbf{F_t}$) respectively, exerted on each pillar. (b) Scanning electron microscopy images of the device. *Fe*-coated PDMS micropillars are 10 µm high, 5 µm in diameter and spaced 2 µm (minimum distance, when $\mu_0 H_e$= 0 mT). On the right: zoom on a single group of 4-pillars. (c) Sketch of a single magnetic pillar with a tri-layer of SiO_2 (50 nm) / *Fe* (150 nm) / SiO_2 (50 nm) deposited on top. (d) Micromagnetic configurations (simulated using OOMMF) of two adjacent *Fe*-disks on top of PDMS pillars, when an external magnetic field ($\mu_0 H_e$= 50 mT) is applied along the *x*-axis. The arrows represent the local magnetization direction, while the red-white-blue scale color refers to the *y*-component of the magnetization. (e-f) Optical microscopy images of two adjacent pillars, comparing the distance between centers without (x_0, panel e) and with (x_1, panel f) the application of $\mu_0 H_e$= 50 mT along the *x*-axis. The dashed circle represents the overlaid position of the pillar on the right in absence of H_e, as in Fig.1e. (g) On the left *y*-axis: experimental (black line) and simulated (red dashed-line) deflection ($\Delta x = x_0 - x_1$) of magnetic pillars as function of the external field ($\mathbf{H_e}$), directed along the line connecting adjacent *Fe*-disks centers (*x*-axis in Fig. 1d). The relatively large uncertainty of experimental data arises from the limited resolution of optical microscopy, combined with shape defects of the pillars, which hinder the 2D fitting for the determination of the center position. On the right *y*-axis: calculation of the *x*-component of the magnetic force ($\mathbf{F_M}$, blue) between two adjacent magnetic pillars as function of $\mathbf{H_e}$. Scale bars: 5 µm (b,f).

$$I_{norm}(t) = \frac{I(t) - I_B}{I_{pre-bleach} - I_B} \bullet \frac{T_{pre-bleach} - I_B}{T(t) - I_B} \qquad (2)$$

where *I(t)* is the measured intensity in the bleached area, I_B is the background intensity, $I_{pre\text{-}bleach}$ is the average intensity before photobleaching in the bleached region, $T_{pre\text{-}bleach}$ the intensity of the whole nucleus before bleaching and *T(t)* the total intensities of the whole nucleus as function of time. The first factor in the equation allows to calculate the recovery fraction, normalizing *I(t)* to the initial value and rescaling it between 0 and 1. The second factor, instead, allows to compensate the general tendency to underestimate the fluorescence recovery in FRAP experiments, due the overall bleaching of the cell, by normalizing the intensity in the bleached area also to the average intensity from the nucleus.

Images Correlation Analysis

A pixel-by-pixel images correlation analysis was performed to investigate RFP-Lifeact (see Fig. 5b) and H2B-EGFP (see the ESI†, section S4 and Fig. S9) dynamics. Starting from a reference frame, we acquired images for 20 minutes, at 3 frames per minute. A 2D correlation coefficient between each frame and the reference one is calculated, according to the following equation:

$$c = \frac{\sum_m \sum_n (A_{mn} - \bar{A})(B_{mn} - \bar{B})}{\sqrt{\left(\sum_m \sum_n (A_{mn} - \bar{A})^2\right)\left(\sum_m \sum_n (B_{mn} - \bar{B})^2\right)}} \quad (3)$$

where *c* is the 2D correlation coefficient, while A_{mn} and B_{mn} are the matrix elements representing the pixels of the two images. A is the image of the reference frame, while B is the image taken at different times during acquisition. $\bar{A}$ and $\bar{B}$ are the average intensity of the two images. The subtraction of the average value reduces the impact of photobleaching on the estimate of the images correlation.

In this way, we calculated for each cell the correlation curve, i.e. the evolution of *c* vs. time (see Fig. 5b and Fig. S9 in the ESI†).

Results and discussion

Magnetic micropillars: working principle and characterization

The concept of the magnetic actuation is illustrated in Fig. 1a, with reference to a single square group of magnetic pillars acting on a cell cultured on top. When a uniform in-plane magnetic field ($\mathbf{H_e}$) is applied along the side of the pillars square, the couples of adjacent pillars along the field direction experience an attractive force, arising from the proximity of magnetic charges of opposite sign. On the other hand, those perpendicular to $\mathbf{H_e}$ feel a repulsive force, produced by the closer proximity of magnetic charges of the same sign (see Fig. 1a). If a rotating field is applied, a continuous bending of the pillars occurs, exerting on cells a periodic and biaxial mechanical stimulus, compressive and tensile along perpendicular directions. Fig. 1b shows an electron microscopy image of the active substrate developed in this paper, consisting in a two-dimensional array of square groups of four polydimethylsiloxane (PDMS) micropillars. The magnetic head shown in Fig. 1c is made of a 150 nm thick *Fe* film, sandwiched by two 50 nm thick SiO_2 layers. For details on the fabrication, see *Materials and Methods*.

To estimate the magnitude of the magnetic forces, let us first consider the basic unit cell of each structure, i.e. a couple of adjacent pillars (see Fig. 1d). Under the application of an in-plane field $\mathbf{H_e}$, two adjacent pillars reciprocally interact, as the magnetization **M** in the first *Fe*-disk produces a magnetic stray field gradient on the second and vice-versa. For $\mu_0 H_e$ ranging between 10 and 100 mT, *Fe*-disks behave as magnetic dipoles in a single domain configuration (see Fig. 1d), with **M** aligned to $\mathbf{H_e}$, as resulting from micromagnetic simulations carried out with the software OOMMF (see *Materials and Methods* and the ESI†, section S1 and Fig. S3a-c). The calculated stray field from the disks has been then used to evaluate the magnetic force $\mathbf{F_M}$ (see *Methods*). According to the physics of dipole-dipole interaction, $\mathbf{F_M}$ is attractive (positive) when $\mathbf{H_e}$ is directed along the line connecting the two pillars centres, while $\mathbf{F_M}$ is repulsive (negative) if $\mathbf{H_e}$ is perpendicular to that direction. For an external field $\mu_0 H_e$= 50 mT (the same used in biological experiments), we found an attractive force F_M = 47.8 nN when the field is oriented along the *x*-axis (see Fig. 1d), and a repulsive force F_M = -13.7 nN for $\mathbf{H_e}$ applied along the *y*-axis. When $\mathbf{H_e}$ is directed at 45 degrees, a lower attractive force F_M = 11.3 nN is exerted. Note that the maximum attracting force is more than three times larger than the repulsive one, indicating that stimuli applied on cells are mainly compressive, similar to a "pinching" at a sub-micron scale.

As expected, F_M increases with H_e because it favours the alignment of **M** along the field direction, resulting in larger magnetic moment of the *Fe*-disks. In Fig. 1g, we report the simulated *x*-component of $\mathbf{F_M}$ (blue line) for a couple of pillars, when a $\mu_0 H_e$ field up to 100 mT is applied along the *x*-axis (see Fig. 1d). The graph shows that F_M increases with the external field, up to 73 nN. This demonstrates the possibility to tune the strength of the force with $\mathbf{H_e}$, thus controlling the entity of pillars bending and, consequently, the mechanical pinching applied on cells.

We measured the effect of $\mathbf{F_M}$ on the pillars deflection by optical microscopy, for variable $\mathbf{H_e}$ applied along the horizontal *x*-direction (see Fig. 1e,f). The deflection (Δx) is measured as the difference between the distance separating the *Fe*-disks centres without field (x_0) and for applied $\mu_0 H_e$ ranging between 25-100 mT (x_1). The centres position is estimated by circular 2D fitting of the *Fe*-disks edges. As shown in Fig. 1g (black line), Δx increases with $\mathbf{H_e}$ up to 620±130 nm for $\mu_0 H_e$= ±100 mT, independently on the field polarity, as expected from the system symmetry. Moreover, the distance between disks centres when $\mathbf{H_e}$ is restored to zero (x_0), does not depend on the sequence of applied fields, in agreement with the negligible remanent magnetization of *Fe*-disks, causing a residual attracting force of just 1.2 nN (see the ESI†, section S1). This is crucial for the reproducibility of the mechanical stimuli applied on cell, as both the initial condition and the applied stress are well defined and controlled only by the external field.

In order to check the consistency between pillars deflections and the strength of simulated forces, we modelled each pillar as a homogeneous cylinder[38]. The deflection is proportional to the force applied to the top of the pillars, i.e. $\Delta x = 2F_M / k$, where $k = (3/64)\pi E D^4/H^3$ is the elastic constant of the pillar, *D* and *H* are pillars diameter and height, respectively, and *E* is the Young modulus. The best fit of the experimental deflections (see red dashed-line in Fig. 1g) is obtained for *E*= 2.56 MPa, slightly larger than the PDMS Young modulus (1.84 MPa)[37], but coherent with the presence of the *Fe*-disks deposited on top and some *Fe* on the side walls, which confers a larger rigidity to the pillars.

Multiple mechanical pinching on individual cells

To test the platform, NIH3T3 fibroblasts were cultured on the micropillars and exposed to mechanical pinching by applying a rotating $\mathbf{H_e}$. Cells spread on few (3-5) 4-pillars groups (see Fig. 2c), thus experiencing multiple stimulations at different points of the plasma membrane. At variance with passive microposts used so far [22,23,24], cells do not significantly alter the pillars' position due to the reduced aspect ratio (see Fig. 1b). Biocompatibility has been assessed on cells cultured on the active substrate for three days. No evident change in viability and proliferation was observed.

During all the experiments a rotating field with amplitude $\mu_0 H_e$= 50 mT was applied. The rotation frequency (f_F) was 0.05 Hz, while the pinching frequency (f_P) was $2 \cdot f_F$ = 0.1 Hz, as the stress field is unchanged upon 180 degrees rotation of $\mathbf{H_e}$ (see frames 1 and 5 in Fig. 2a). In order to properly visualize the mechanical-pinching, pillars were coated with fluorescent Cy5-fibronectin. Fig. 2a shows the frames from a video (see the ESI† Movie 1), illustrating the different configurations of a group of 4-pillars, during the mechanical stimulation of a fibroblast. When $\mathbf{H_e}$ rotates, depending on the field orientation, a time-varying stress field is exerted on the cell, as pictorially depicted in Fig. 2b. In frame 1, for $\mathbf{H_e}$ directed along *x*, a compressive (tensile) stress is applied along *x* (*y*); the pillars define a rectangle (dashed line in Fig. 2a) stretched along *y*. Rotating $\mathbf{H_e}$ counter-clockwise, at 45 degrees with respect to *x*, a weaker compressive stress, both along *x* and *y*, is applied (frame 2). Again, a biaxial stress like that of frame 1, but rotated by 90 degrees, is obtained for $\mathbf{H_e}$ at 90 degrees with respect to *x* (frame 3). By rotating the field up to 135 and 180 degrees, the configurations of frames 4 and 5 are produced, which by symmetry are the very same of frames 2 and 1, respectively.

To highlight the dependence of the force on the field direction, the simulated magnetic force acting on each pillar is plotted (see Fig. 2d) as a function of the angle between the field and the x-axis (ϕ). For a rotating applied field with amplitude $\mu_0 He$= 50 mT, the force components (F_x and F_y) are periodic in ϕ and the simulated values are well fitted by sine functions (see Fig. 2d). As expected, the maximum of the *x*-component (F_x = 47.8 nN) is found for ϕ= 0 degrees, while at 90 degrees the force is less intense but repulsive (F_x = -13.7 nN). By symmetry, F_y is equivalent to F_x, with a phase shift of 90 degrees. Note that, the force acting on a single pillar is calculated (see *Materials and Methods*) just by considering the interaction between first neighboring pillars and neglecting the one along the diagonal of the square, which results in a negligible contribution (~2 nN, see the ESI†, section S1).

It is worth mentioning that the force applied to the cell membrane is lower than the magnetic force reported above, as part of it is needed to deform the pillars. A rough estimate of the maximum mechanical force applied in our experimental conditions, however, gives a value of ~20 nN (see the ESI†, section S1). In turns, the maximum strain applied to the cell, assuming that the cell membrane locally follows the displacement of the disks as in Fig. 2a, is about 5%. This value is coherent with the typical strain experienced by fibroblasts in-vivo[39].

Periodic pinching affects nuclear morphology

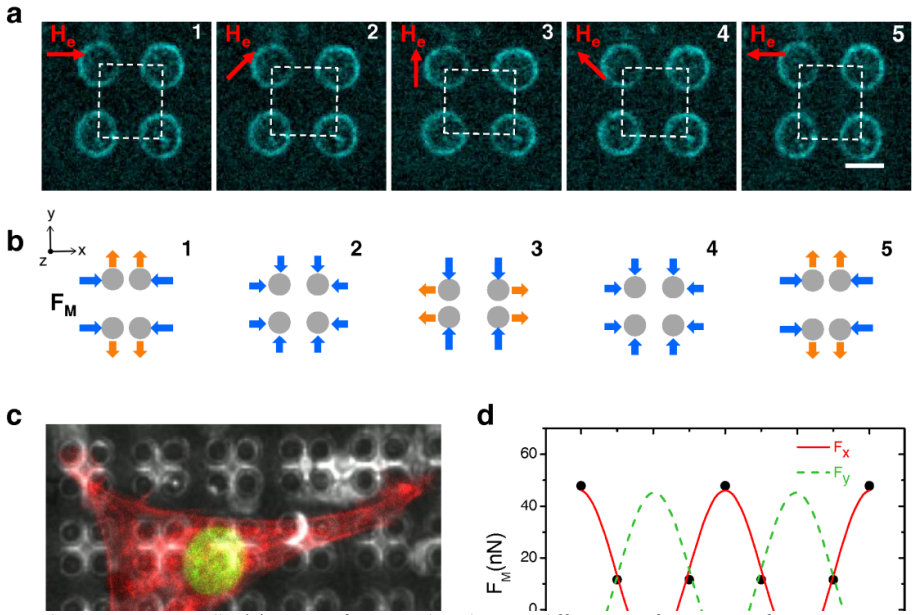

Fig. 2 Magnetic pillars exert pinching on NIH3T3 cells. (a) Frames from a video showing different configurations of a square group of magnetic pillars with a fibroblast cell plated on top, when a rotating $\mu_0 H_e$= 50 mT is applied. Pillars, coated with Cy5-fluorescent fibronectin, sequentially attract and repel in vertical and horizontal directions according to the orientation of $\mathbf{H_e}$. (b) Scheme of the forces exerted on a group of four pillars. The blue (and orange) arrows represent the direction of the attractive (and repulsive) force components exerted on the cell by each pillar. (c) Optical image showing the device with the magnetic *Fe*-coated pillars and a single NIH3T3 cell transfected with RFP-Lifeact (red fluorescence) and H2B-EGFP (green fluorescence). (d) Simulations of the magnetic force ($\mathbf{F_M}$) exerted on magnetic pillars, as function of the field direction ($\mathbf{H_e}$), when a rotating $\mu_0 H_e$= 50 mT is applied. The simulated data (black dots) are fitted with a sinusoidal curve for the *x*-component (F_x, red-line). By symmetry, the *y*-component (F_y, dashed green-line) has the same behavior of F_y, but displays a phase shift of 90 degrees. Scale bars: 5 µm (a), 20 µm (c).

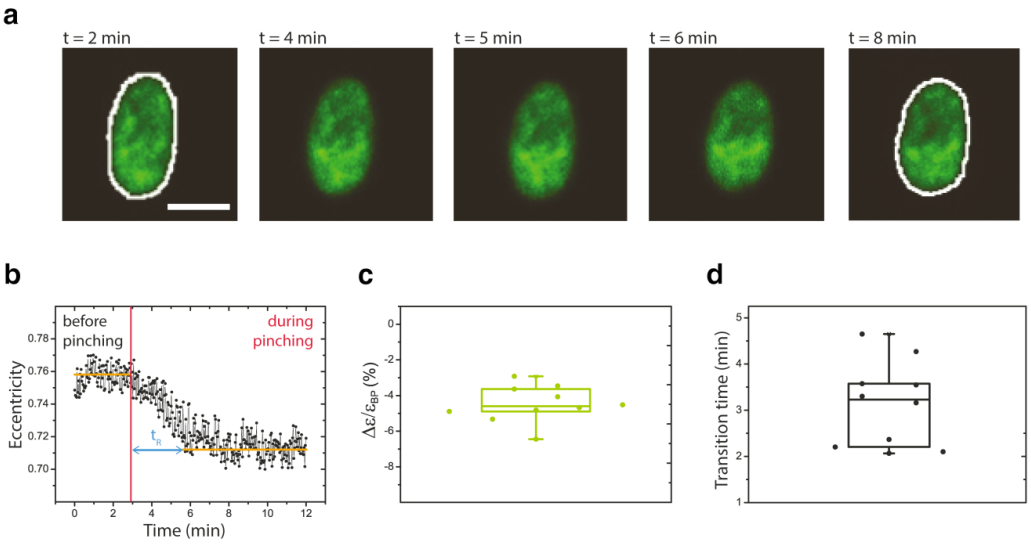

Fig. 3 M …P green fluoresc …mes less elongat …rojected area ec …o a less elongated state. The orange lines represent the average eccentricity before and during pinching. (c) Box plot for the percentage nucleus projected area eccentricity variation $\Delta\varepsilon_R = \frac{\varepsilon_{DP}-\varepsilon_{BP}}{\varepsilon_{BP}}$, where ε_{BP} and ε_{DP} are respectively the average eccentricity before pinching (t= 0-3 min, see Fig. 3b) and during pinching (t= 9-12 min). $\Delta\varepsilon_R$ is calculated for a batch of n= 10 cells (data acquired in three different experiments). The bottom and top of the box represent the first and third quartiles, whereas the line inside the box represents the median. The ends of the whiskers correspond to the lowest/highest data point of the distribution. (d) Box plot for the transition time (t_R) of the nucleus projected area to a lower eccentricity "quasi stationary state" (see Fig. 3b), extrapolated (see the ESI†, Fig. S6) by a batch of n= 10 cells. The bottom and top of the box represent the first and third quartiles, whereas the line inside the box represents the median. The ends of the whiskers correspond to the lowest/highest data point of the distribution. Scale bar: 5 µm.

As shown in previous works[40,41] the application of forces and the alteration of substrates stiffness can affect the shape of the cell nucleus. For this reason, we first investigated the impact of periodic pinching by magnetic pillars on the nuclear morphology. As quantitative indicator of the cell nucleus morphology, we use the eccentricity (ε) of the nuclei projected area, extracted from fluorescence H2B-EGFP images (see *Methods*). H2B is a core histone, a nuclear protein responsible for the chromatin structure. The cells are imaged for 3 minutes before application of the mechanical stimulus, under a static $\mathbf{H_e}$ at 45 degrees, producing a weak compressive stress both along x and y (see frame 2 in Fig. 2a). Subsequently, cells undergo pillars stimulations and are imaged for 9 minutes with an acquisition rate of 0.5 frames per second (fps). Frames reported in Fig. 3a show that the nucleus appears less elongated under mechanical stimulation (t = 8 min) than before (t = 2 min) and the corresponding eccentricity as function of time is plotted in Fig. 3b. The average eccentricity before pinching (ε_{BP}), from 0 to 3 min is 0.76, while during pinching it decreases to ε_{DP}= 0.72. ε_{DP} is calculated as the average eccentricity between 9 and 12 min, in order to discard the transitory when the cell is adapting to the dynamic substrate. Remarkably, the same behavior is observed in all the 10 cells studied (see the ESI†, Fig. S5). Although the initial value of the eccentricity is different for each nucleus, the relative variation of ε, averaged over the 10 cases investigated, turns out to be $\Delta\varepsilon_R$= 4.5±1 % (see Fig. 3c). This suggests a sizable reduction of nuclear tension in response to periodic mechanical stimuli.

The nuclear transition to a less elongated state happens with intrinsic dynamics, characterized by a transition time (t_R) required to the nucleus to adapt its shape, moving from a first "quasi" stationary eccentricity before pinching to a second "quasi" stationary value of ε during pinching (see Fig. 3b). The transition time measured (see the ESI†, Fig. S6) for 10 cells is reported in Fig. 3d and the average value of t_R is 3.1 min, much longer than the pinching period (T_P = 10 s). These findings indicate that the nuclear response is not directly and elastically coupled to the mechanical stimuli applied to the cell membrane. Transmission appears mediated by active and slower cellular processes, as detailed in the next sections.

Periodic mechanical stimulation affects nuclear and chromatin dynamics

Alterations of nuclear shape, such as those presented above, are related to modifications in the nucleus-cytoskeleton coupling[42,43] which can also induce changes in nuclear motility and deformability. In order to elucidate this aspect, we investigated the effect of a periodic pinching on nuclear plasticity by monitoring the nuclear area fluctuations, according to a procedure recently developed by some of the authors[26]. Individual H2B-EGFP positive cells were imaged (at 3 frames per minute) for 30 min before and during mechanical pinching.

From each video, we extracted the percentage nuclear area fluctuations (PNAF) vs. time, defined as the fluctuations from the mean value of the nuclei projected area (see *Materials and Methods*), which provide information on the nucleus plasticity and deformability. In Fig. 4a the PNAFs for a single cell are reported, where an enhancement of the nuclear fluctuations during pinching is observed. A control experiment on pillars without *Fe* coating, showed no relevant variation of PNAFs induced by the rotating magnetic field (see the ESI†, Fig. S7b), thus confirming that the effect is due to the mechanical stimulation of the pillars. Fig. 4b shows the statistical distribution of PNAFs, measured on 10 different cells (see the ESI†, Fig. S7a), before (black) and during (red) pinching. Remarkably, the distribution of PNAFs during mechanical stimulation is broader than that before, with a standard deviation (σ_{DP}= 1.3%) which is more than two times larger than before pinching (σ_{BP}= 0.5%). The analysis of PNAFs shows that cellular nucleus deformability increases, indicating a reduction of nuclear pre-stress during stimulation. Furthermore, the time evolution of area fluctuations can be used to investigate the nature of the coupling between the periodic mechanical stimulus and the nuclear response. To this scope, we estimated the correlation coefficient (see the ESI†, section S3 and Fig. S8) between the normalized nuclear area fluctuations vs. time (acquired at 0.5 fps) and the applied stress field giving by pinching (at f_p = 0.1 Hz). As a matter of fact, the two curves are uncorrelated, demonstrating that the nuclear fluctuations are not directly linked to the stress field oscillations. Indeed, the elastic coupling between the cell membrane and the nucleus is weak, coherently with the slow dynamics of the nuclear shape transition reported above. This points out the role of active cellular processes for the transfer of the stimulus to the nucleus.

Beside the dynamics of nuclear morphology, we studied the impact of pinching on protein dynamics inside the nucleus. To this scope, we performed FRAP (Fluorescence recovery after photobleaching) on H2B-EGFP positive cells. The procedure (see *Materials and Methods*) consists in measuring the fluorescence recovery in a certain area of the nucleus (a circle with a diameter of 4 µm), after photobleaching of that region with high laser intensity. In Fig. 4c, we compare the normalized intensity in the bleached area

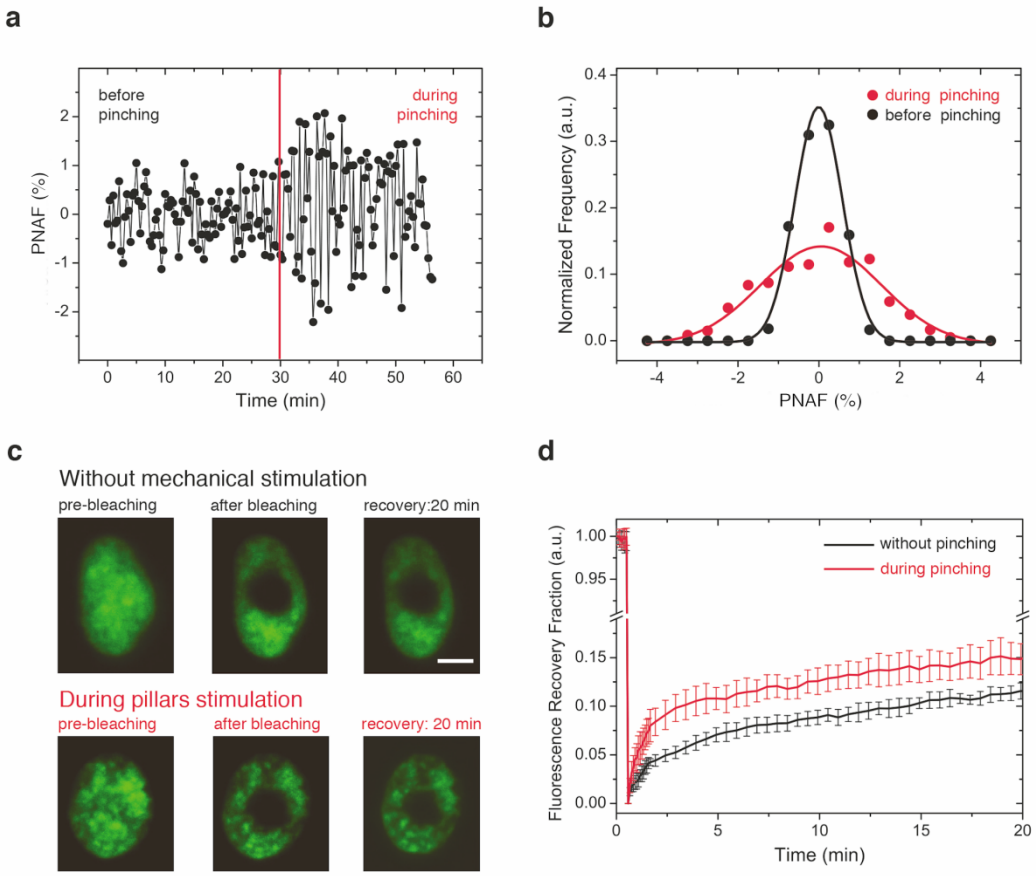

Fig. 4 Magnetic pillars stimulation affects nuclear area fluctuations and H2B dynamics. (a) Percentage nuclear area fluctuations (PNAFs) vs time of a cell before and during pinching. The red line represents the time at which rotation of $\mu_0 H_e$= 50 mT is turned on. (b) Black and red dots represent the distribution of combined percentage nuclear area fluctuations (PNAFs) for n= 10 cells and all the time points, before and during pinching respectively (data acquired in four different experiments). In order to disregard transitory effects, the statistics is related to data acquired from 10 to 30 min after the field rotation is turned on. Continuous lines are Gaussian fittings. (c) Frames showing H2B-EGFP fluorescence intensity upon photobleaching and recovery, without and with mechanical pinching of cells. The bleached ROI is a circle with a diameter of 4 µm. (d) Fluorescence recovery curves for nuclear H2B-EGFP signal (mean on n= 10 cells), without (black) and with (red) the application of a rotating $\mu_0 H_e$= 50 mT (data acquired in four different experiments). The error bars represent the standard deviations from the mean. Scale bar: 5 µm.

Fig. 5 Magnetic pillars stimulation induces actin reorganization and MKL translocation. (a) Frames from a video showing a NIH3T3 cell (RFP-Lifeact red fluorescence), during an experiment. The cell is imaged for 40 minutes, before (0-20 min) and during (20-40 min) mechanical pinching. Upon application of a rotating field ($\mu_0 H_e$= 50 mT) at t= 20 min, faster actin dynamics are observed. (b) Images correlation vs time of RFP-Lifeact red fluorescent signal from reference frame, before (black, reference frame at t= 0 min) and during (red, reference frame at t= 20 min) pinching, calculated for n= 10 cells. The correlation coefficient is calculated according to Equation 3, performing a pixel-by-pixel analysis. The reference frames during pinching corresponds to the time point at which the field rotation ($\mu_0 H_e$= 50 mT) is turned on. Error bars represent the standard deviations from the mean. The inset shows box plots for the linear fitting of images correlation coefficient slopes (dc/dt), calculated for 10 cells before (black) and during (red) pinching (see the ESI† Fig. S10). The bottom and top of the box represent the first and third quartiles, whereas the line inside the box represent the median. The ends of the whiskers correspond to the lowest/highest data point of the distribution. (c) Optical images showing mcherry-MKL signal in the cell nucleus and cytoskeleton, before and during the mechanical stimulation. The rotating field ($\mu_0 H_e$= 50 mT) is applied for 30 min before the acquisition of the second frame. (d) Color map of MKL signal, subtraction the intensity during (I_{DP}) and before (I_{BP}) pinching. (e) Box plots for the MKL relative intensity, calculated as the ratio between the intensity during and before pinching (I_{DP}/I_{BP}) for n= 10 cells, respectively in the nucleus (blue) and cytoplasm (green). The MKL intensity both inside the nucleus and in the cytoplasm is calculated as the average of 5 different circular ROIs with a diameter of 2 µm. The bottom and top of the box represent the first and third quartiles, whereas the line inside the box represents the median. The ends of the whiskers correspond to the lowest/highest data point of the distribution. Scale bars: 20 µm (a,c).

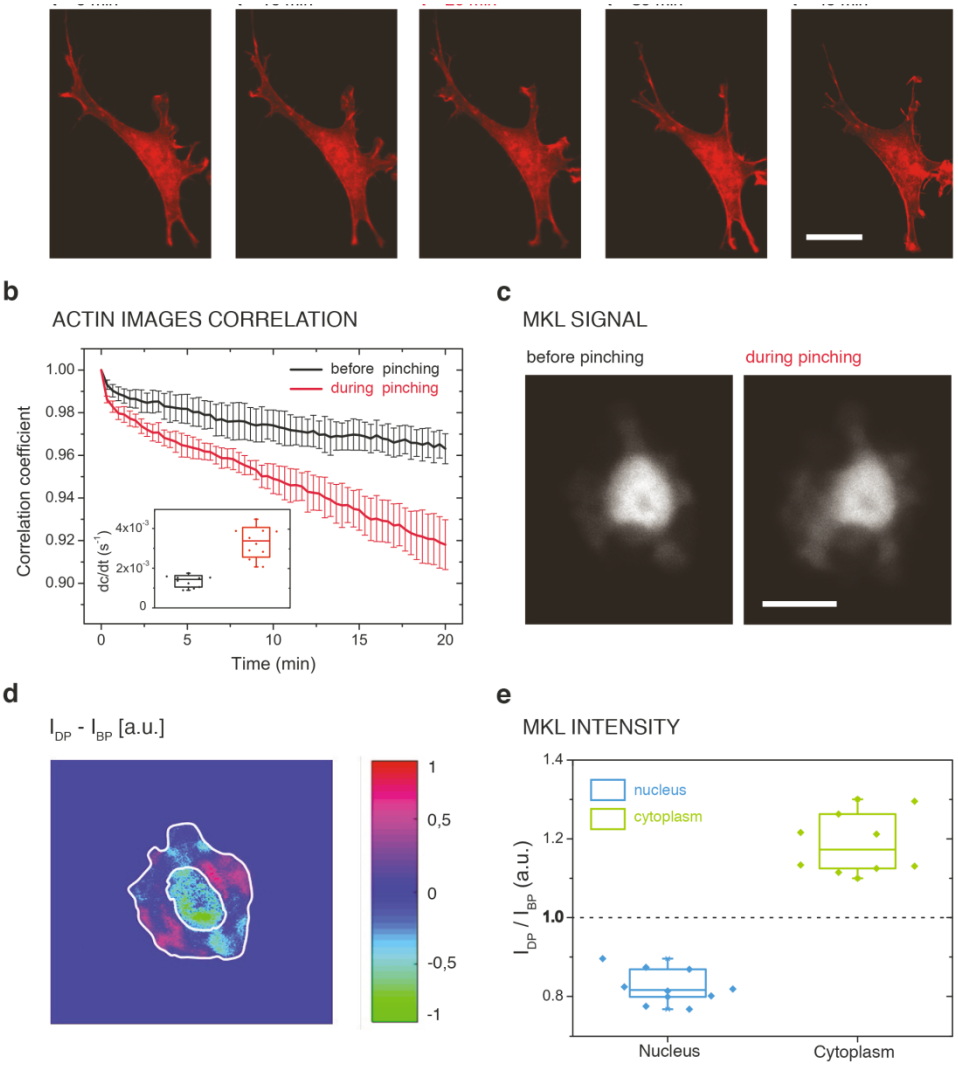

vs time, in cells subjected/not-subjected to mechanical pinching, bottom and top panels, respectively. The recovery fraction (see Fig. 4d), calculated on 10 different nuclei, is faster during pinching, especially immediately after bleaching. This indicates a higher diffusivity and enhanced dynamics of H2B histone inside the nucleus during stimulation, thus suggesting that mechanical stimulation leads to a relatively more decondensed chromatin structure. The enhancement in H2B core-histone dynamics is also confirmed by H2B images correlation analysis, which shows an increased decorrelation of H2B signal during pinching (see *Materials and Methods* and the ESI†, section S4).

Pinching induces Actin reorganization and MKL cofactor translocation

To investigate the role of active cellular processes, responsible for the transmission of mechanical stimuli from the pillars to the nucleus, we first studied the effect of such stimuli on actin, one of the most abundant proteins in the cytoskeleton[44]. Fig. 5a represents a cell transfected with RFP-Lifeact and imaged for 20 minutes before and after the activation of pinching. The images show sizable variations of the cell morphology during stimulation, while reduced

dynamics are observed before pinching. To put this finding on a quantitative basis, we performed RFP-Lifeact images correlation analysis (see *Materials and Methods*), both before and during pinching. It involves a pixel-by-pixel correlation of RFP-Lifeact maps, taken at 3 frames per minute, with the initial time frame (at t= 0 min for data before pinching and at t= 20 min for data during pinching). Then, the correlation coefficient is calculated for each cell as a function of time. In Fig. 5b we compare the average correlation coefficient from 10 different cells (see the ESI†, Fig. S10), before (black curve) and after (red curve) the application of mechanical pinching. By performing a linear fit of the two curves, it is possible to quantify the faster decay of the correlation coefficient during stimulation, with a slope (see the inset in Fig. 5b) 2.4 times higher than in the static case. An enhancement in actin images de-correlation is therefore observed during pinching. This demonstrates that the periodic mechanical stimuli exerted by the pillars affects actin dynamics, pointing out the role played by the cytoskeleton in the mechanical signal transmission towards the nucleus, not via direct mechanical coupling but through the reorganization of actin upon mechanical stimulation.

Finally, we investigated the effect of the mechanical stimuli on *megakaryoblastic acute leukemia factor-1* (MKL) translocation. MKL is a transcription cofactor, located in both the nucleus and cytoplasm, which can shuttle between the two, in response to mechanical stimuli, thus bringing about alterations in gene transcription. Recent studies[16,45,46] have demonstrated that the actin configuration is related to MKL translocation. MKL moves to the cytoplasm when actin fibers are depolymerized while a translocation to the nucleus occurs when actin polymerizes into fibers. During the experiments, we imaged cells before the mechanical stimulation and after 30 min from the activation of periodic pinching. The images in Fig. 5c show that MKL cofactor shuttles outside the nucleus in response to the mechanical stimuli. To better visualize the MKL translocation we subtracted the intensity map of MKL before pinching from that during pinching (I_{DP}-I_{BP}) and this difference is shown in Fig. 5d. Moreover, we report the average MKL intensity ratio I_{DP}/I_{BP} during and before pinching, both inside and outside the nucleus, from data acquired on 10 different cells (see Fig. 5e). Data report an increase of the intensity ratio in the cytoplasm (I_{DP}/I_{BP}= 1.19) and a decrease in the nucleus (I_{DP}/I_{BP}= 0.83) when cells are pinched, thus showing that MKL translocates out of the nucleus. This mechanism provides a possible path for mechanical stimuli to induce changes in gene expression by regulating shuttling of transcription factors/co-factors. Remarkably, MKL translocation to the cytoplasm suggests actin depolymerization in response to cell pinching. This is in agreement with our findings on nucleus morphology and dynamics, as a less elongated and more dynamic nucleus reflects a reduction of the mechanical stress induced by the cytoskeleton, as expected by a depolymerized actin configuration[26].

Conclusions

In this paper we present a novel platform for in-vitro application of mechanical stimuli with tunable spatio-temporal profile at different points of the cell membrane. It consists in an active substrate for cell culture, made of groups of PDMS pillars with magnetic heads, whose deflection can be controlled at the nanometre scale by external magnetic fields. A rotating magnetic field produces a periodic biaxial strain field, corresponding to a pinching of the cell at the adhesion points. For platform validation, we have studied the NIH3T3 cell response at a fixed pinching frequency of 0.1 Hz, corresponding to a maximum strain of 5% on cells. We found that this periodic stimulation induces changes in nuclear morphology, deformability and H2B core histone dynamics. Remarkably, the nuclear response to such external forces does not result from a purely elastic coupling between the cell membrane and the nucleus, but involves active cellular processes, such as actin reorganization and MKL cofactor translocation.

The sinusoidal pinching considered here is just the basic component of any mechanical stimulation with complex temporal profile, which could be produced by tuning the time-shape of the uniform external field applied to the whole chip. Furthermore, the synchronous motion of all groups of pillars enables the parallel stimulation of all cells plated on the chip, thus paving the way to the investigation of the impact of mechanical stimulation on collective cellular phenomena.

In perspective, by proper scale up or down of the size of magnetic pillars and temporal modulation of the external magnetic field, our method can be exploited in a large variety of biological studies, from single cells to tissues, where the application of localized forces with tunable temporal profile is required.

Conflicts of interest

There are no conflicts to declare.

Acknowledgements

We thank E. Albisetti, P.P. Sharma, D.V. Conca and A. Ravasio for the fruitful discussions. M.M. thanks G. D'Abrosca for her skilful graphic support. M.M., D.S.J. and G.V.S. thank "MBI microscopy core" for the optical components they provided and "MBI wet lab core" for actively maintaining the cell culture room that was used. M.M., D.P. and R.B. thank C. Somaschini and G. Iseni for the technical support. This work was funded by MIUR via the project “ATR and ATM-mediated control of chromosome integrity and cell plasticity” (Project No. 2015SJLMB9) and by Fondazione Cariplo via the project UMANA (Project No. 2013-0735). The fabrication of the devices was performed at PoliFab, the micro- and nanofabrication facility of "Politecnico di Milano".

References

1. Mitchell, M. J., Jain, R. K. & Langer, R. Engineering and physical sciences in oncology: challenges and opportunities. Nature Rev. Cancer, 17, 659-675 (2017).
2. Cross, S. E., Jin, Y. S., Rao, J. & Gimzewski, J. K. Nanomechanical analysis of cells from cancer patients. Nat. Nanotechnol. **2**, 780-83 (2007).
3. Wirtz, D., Konstantopoulos, K. & Searson, P. C. The physics of cancer: the role of physical interactions and mechanical forces in metastasis. Nature Rev. Cancer **11**, 512–522 (2011).
4. Fedosova, D. A., Caswella, B., Sureshc, S. & Karniadakisa, G. E. Quantifying the biophysical characteristics of Plasmodium-

falciparum-parasitized red blood cells in microcirculation. Proc. Natl. Acad. Sci. USA **1**, 35-39 (2011).
5. Khatau, S. B. et al. The distinct roles of the nucleus and nucleus–cytoskeleton connections in three-dimensional cell migration. Sci. Rep. **2**, 488 (2012).
6. Lee, J. S. H. et al. Nuclear lamin A/C deficiency induces defects in cell mechanics, polarization, and migration. Biophys. J. **93**, 2542–2552 (2007).
7. Roca-Cusachs, P. et al. Micropatterning of single endothelial cell shape reveals a tight coupling between nuclear volume in G1 and proliferation. Biophys. J. **94**, 4984–4995 (2008).
8. Jain, N., Iyer, K. V., Kumar, A. & Shivashankar, G. V. Cell geometric constraints induce modular gene-expression patterns via redistribution of HDAC3 regulated by actomyosin contractility. Proc. Natl Acad. Sci. USA **110**, 11349–11354 (2013).
9. Wang, N., Tytell, J. D. & Ingber, D. E. Mechanotransduction at a distance: mechanically coupling the extracellular matrix with the nucleus. Nat Rev Mol Cell Bio, 10, 75-82 (2009).
10. Shivashankar, G. V. Mechanosignaling to the Cell Nucleus and Gene Regulation. Annual Review of Biophysics, 40, 361-378 (2011).
11. Cho, S., Irianto, J., & Discher, D. E. Mechanosensing by the nucleus: From pathways to scaling relationships. J. Cell Bio., **216**, 305-315 (2017).
12. Dahl, K. N., Engler, A. J., Pajerowski, J. D. & Discher, D. E. Power-law rheology of isolated nuclei with deformation mapping of nuclear substructures. Biophys. J. **89**, 2855–2864 (2005).
13. Celedon, A., Hale, C. M. & Wirtz, D. Magnetic Manipulation of Nanorods in the Nucleus of Living Cells. Biophys J. **19**, 1880–1886 (2011).
14. Monticelli, M. et al. Magnetic domain wall tweezers: a new tool for mechanobiology studies on individual target cells. Lab Chip, 2882-2890, (2016).
15. Tajik, A. et al. Transcription upregulation via force-induced direct stretching of chromatin. Nature Materials. **15**, 1287-1296 (2016).
16. Iyer, K. V., Pulford, S., Mogilner, A. & Shivashankar, G. V. Mechanical activation of cells induces chromatin remodeling preceding MKL nuclear transport. Biophysical Journal. **103**, 7, 1416-1428, (2012).
17. Ashkin, A., Dziedzic, J. & Yamane, T. Optical trapping and manipulation of single cells using infrared laser beams. Nature **330**, 769–771 (1987).
18. Ivanovska, I., Swift, J., Harada, T., Pajerowski, J. D. & Discher, D. E. Physical plasticity of the nucleus and its manipulation. Methods Cell Biol. **98**,207–220 (2010).
19. Guilak, F., Tedrow, J. R. & Burgkart, R. Viscoelastic properties of the cell nucleus. Biochem. Biophys. Res. Commun. **269**, 781–786 (2000).
20. Lombardi, M. L. & Lammerding, J. Altered mechanical properties of the nucleus in disease. Methods Cell Biol. **98**, 121–141 (2010).
21. Lammerding, J. & Lee, R. T. Mechanical properties of interphase nuclei probed by cellular strain application. Methods Mol. Biol. **464**, 13–26 (2009).
22. [1] Liu, Z., Liu, Y., Chang, Y., Seyf, H. R., Henry, A., Mattheyses et al. Nanoscale optomechanical actuators for controlling mechanotransduction in living cells. Nature methods, 13(2), 143 (2015).
23. Davidson, P. M., Özçelik, H., Hasirci, V., Reiter, G. & Anselme, K. Microstructured surfaces cause severe but non-detrimental deformation of the cell nucleus. Adv. Mater. **21**, 3586–3590 (2009).
24. Badique, F. et al. Directing nuclear deformation on micropillared surfaces by substrate geometry and cytoskeleton organization. Biomaterials **34**, 2991–3001 (2013).
25. Pan, Z. et al. Control of cell nucleus shapes via micropillar patterns. Biomaterials **33**, 1730–1735 (2012).
26. Versaevel, M., Grevesse, T. & Gabriele, S. Spatial coordination between cell and nuclear shape within micropatterned endothelial cells. Nature Commun. **3**, 671 (2012).
27. Makhija, E., D. S. Jokhun, D. S. & G. V. Shivashankar, G. V. Nuclear deformability and telomere dynamics are regulated by cell geometric constraints. PNAS. **113**, E32-40 (2016).
28. Fu, Y., Chin, L. K., Bourouina, T., Liu, A. Q. & VanDongen, A. M. J. Nuclear deformation during breast cancer cell transmigration. Lab Chip. **12**, 3774–3778 (2012).
29. Xu, F., et al. A microfabricated magnetic actuation device for mechanical conditioning of arrays of 3D microtissues. Lab Chip. **15**, 2496–2503 (2015).
30. Digabel, J.,Biais, N., Fresnais, J., Berret, J. F., Hersen, P., & Ladoux, B. Magnetic micropillars as a tool to govern substrate deformations. Lab Chip. **11**, 2630 (2011).
31. Sniadecki, N. J., et al. Magnetic microposts as an approach to apply forces to living cells. PNAS, **104**, 14553–14558 (2007).
32. Nagayama, K., Inoue, T., Hamada Y., & Matsumoto, T. A novel patterned magnetic micropillar array substrate for analysis of cellular mechanical responses. Journal of Biomechanics. **65,** 194–202 (2017).
33. Bidan, C.M., et al. Magneto-active substrates for local mechanical stimulation of living cells. Sci. Rep. **8**, 1464 (2018)
34. Yang, B., Lieu, Z. Z., Wolfenson, H., Hameed, F. M., Bershadsky A. D., & Sheetz, M. P. Mechanosensing Controlled Directly by Tyrosine Kinases. Nano Lett. **16**, 5951–5961 (2016).
35. Bao G, Suresh S (2003) Cell and molecular mechanics of biological materials. *Nat mater* 2(11):715-725.
36. D. Donahue, OOMMF User's Guide, Version 1.0.Interagency Report NISTIR, 6376, 3 (2004).
37. Landau, L., & Lifshitz, E. Electrodynamics of Continuous Media, Pergamon Press, (1960).
38. Ghibaudo, M., Saez, A., et al. Tranction forces and rigidity sensing regulate cell functions. *Soft Matter* 4, 1836-1843 (2008).
39. Guenat, O.T., & Berthiaume, F. Incorporating mechanical strain in organs-on-a-chip: Lung and skin. *Biomicrofluidics*, 12,4, 042207 (2018).
40. Belmont, A.S., F.M. Kendall, & C.A. Nicolini. Coupling of nuclear morphometry to cell geometry and growth in human fibroblasts. Cell Biophys. **2**, 165-75 (1980).
41. Li, Q., et al., The regulation of dynamic mechanical coupling between actin cytoskeleton and nucleus by matrix geometry. Biomaterials. **35**, 3, 961-9 (2014).
42. Lovett, D.B., Shekhar, N., Nickerson, J.A., Roux, K.J. & Lele, T.P. Modulation of Nuclear Shape by Substrate Rigidity. Cell Mol Bioeng. **6**, 2, 230-238 (2013).
43. Vishavkarma, R. et al. Role of Actin Filaments in Correlating Nuclear Shape and Cell Spreading. PLoS One. **9**, 9, e107895 (2014).
44. Lodish, H. et al. Molecular Cell Biology. 4th edition, New York: W. H. Freeman (2000).
45. Vartiainen, M.K., Guettler, S., Larijani, B. & Treisman, R. Nuclear actin regulates dynamic subcellular localization and activity of the SRF cofactor MAL. Science. **316**, 1749–1752 (2007).
46. Miralles, F., Posern, G., Zaromytidou, A. I. & Treisman, R. Actin dynamics control SRF activity by regulationof its coactivator MAL. Cell. **113**, 3, 329-342 (2003).

[1] Mitchell, M. J., Jain, R. K. & Langer, R. Engineering and physical sciences in oncology: challenges and opportunities. Nature Rev. Cancer, 17, 659-675 (2017).
[2] Cross, S. E., Jin, Y. S., Rao, J. & Gimzewski, J. K. Nanomechanical analysis of cells from cancer patients. Nat. Nanotechnol. **2**, 780-83 (2007).
[3] Wirtz, D., Konstantopoulos, K. & Searson, P. C. The physics of cancer: the role of physical interactions and mechanical forces in metastasis. Nature Rev. Cancer **11**, 512–522 (2011).
[4] Fedosova, D. A., Caswella, B., Sureshc, S. & Karniadakisa, G. E. Quantifying the biophysical characteristics of Plasmodium-falciparum-parasitized red blood cells in microcirculation. Proc. Natl. Acad. Sci. USA **1**, 35-39 (2011).
[5] Khatau, S. B. et al. The distinct roles of the nucleus and nucleus–cytoskeleton connections in three-dimensional cell migration. Sci. Rep. **2**, 488 (2012).
[6] Lee, J. S. H. et al. Nuclear lamin A/C deficiency induces defects in cell mechanics, polarization, and migration. Biophys. J. **93**, 2542–2552 (2007).
[7] Roca-Cusachs, P. et al. Micropatterning of single endothelial cell shape reveals a tight coupling between nuclear volume in G1 and proliferation. Biophys. J. **94**, 4984–4995 (2008).
[8] Jain, N., Iyer, K. V., Kumar, A. & Shivashankar, G. V. Cell geometric constraints induce modular gene-expression patterns via redistribution of HDAC3 regulated by actomyosin contractility. Proc. Natl Acad. Sci. USA **110**, 11349–11354 (2013).
[9] Wang, N., Tytell, J. D. & Ingber, D. E. Mechanotransduction at a distance: mechanically coupling the extracellular matrix with the nucleus. Nat Rev Mol Cell Bio, **10**, 75-82 (2009).
[10] Shivashankar, G. V. Mechanosignaling to the Cell Nucleus and Gene Regulation. Annual Review of Biophysics, 40, 361-378 (2011).
[11] Cho, S., Irianto, J., & Discher, D. E. Mechanosensing by the nucleus: From pathways to scaling relationships. J. Cell Bio., **216**, 305-315 (2017).
[12] Dahl, K. N., Engler, A. J., Pajerowski, J. D. & Discher, D. E. Power-law rheology of isolated nuclei with deformation mapping of nuclear substructures. Biophys. J. **89**, 2855–2864 (2005).
[13] Celedon, A., Hale, C. M. & Wirtz, D. Magnetic Manipulation of Nanorods in the Nucleus of Living Cells. Biophys J. **19**, 1880–1886 (2011).
[14] Monticelli, M. et al. Magnetic domain wall tweezers: a new tool for mechanobiology studies on individual target cells. Lab Chip, 2882-2890, (2016).
[15] Tajik, A. et al. Transcription upregulation via force-induced direct stretching of chromatin. Nature Materials. 15, 1287-1296 (2016).
[16] Iyer, K. V., Pulford, S., Mogilner, A. & Shivashankar, G. V. Mechanical activation of cells induces chromatin remodeling preceding MKL nuclear transport. Biophysical Journal. **103**, 7, 1416-1428, (2012).
[17]Ashkin, A., Dziedzic, J. & Yamane, T. Optical trapping and manipulation of single cells using infrared laser beams. Nature **330**, 769–771 (1987).
[18] Ivanovska, I., Swift, J., Harada, T., Pajerowski, J. D. & Discher, D. E. Physical plasticity of the nucleus and its manipulation. Methods Cell Biol. **98**,207–220 (2010).
[19] Guilak, F., Tedrow, J. R. & Burgkart, R. Viscoelastic properties of the cell nucleus. Biochem. Biophys. Res. Commun. **269**, 781–786 (2000).
[20] Lombardi, M. L. & Lammerding, J. Altered mechanical properties of the nucleus in disease. Methods Cell Biol. **98**, 121–141 (2010).
[21] Lammerding, J. & Lee, R. T. Mechanical properties of interphase nuclei probed by cellular strain application. Methods Mol. Biol. **464**, 13–26 (2009).
[22] Liu, Z., Liu, Y., Chang, Y., Seyf, H. R., Henry, A., Mattheyses et al. Nanoscale optomechanical actuators for controlling mechanotransduction in living cells. Nature methods, 13(2), 143 (2015).
[23] Davidson, P. M., Özçelik, H., Hasirci, V., Reiter, G. & Anselme, K. Microstructured surfaces cause severe but non-detrimental deformation of the cell nucleus. Adv. Mater. **21**, 3586–3590 (2009).
[24] Badique, F. et al. Directing nuclear deformation on micropillared surfaces by substrate geometry and cytoskeleton organization. Biomaterials **34**, 2991–3001 (2013).
[25] Pan, Z. et al. Control of cell nucleus shapes via micropillar patterns. Biomaterials **33**, 1730–1735 (2012).
[26] Versaevel, M., Grevesse, T. & Gabriele, S. Spatial coordination between cell and nuclear shape within micropatterned endothelial cells. Nature Commun. **3**, 671 (2012).
[27] Makhija, E., D. S. Jokhun, D. S. & G. V. Shivashankar, G. V. Nuclear deformability and telomere dynamics are regulated by cell geometric constraints. PNAS. **113**, E32-40 (2016).
[28] Fu, Y., Chin, L. K., Bourouina, T., Liu, A. Q. & VanDongen, A. M. J. Nuclear deformation during breast cancer cell transmigration. Lab Chip. **12**, 3774–3778 (2012).
[29] Xu, F., et al. A microfabricated magnetic actuation device for mechanical conditioning of arrays of 3D microtissues. Lab Chip. **15**, 2496–2503 (2015).
[30] Digabel, J.,Biais, N., Fresnais, J., Berret, J. F., Hersen, P., & Ladoux, B. Magnetic micropillars as a tool to govern substrate deformations. Lab Chip. **11**, 2630 (2011).
[31] Sniadecki, N. J., et al. Magnetic microposts as an approach to apply forces to living cells. PNAS, **104**, 14553–14558 (2007).
[32] Nagayama, K., Inoue, T., Hamada Y., & Matsumoto, T. A novel patterned magnetic micropillar array substrate for analysis of cellular mechanical responses. Journal of Biomechanics. **65,** 194–202 (2017).
[33] Bidan, C.M., et al. Magneto-active substrates for local mechanical stimulation of living cells. Sci. Rep. **8**, 1464 (2018)
[34] Yang, B., Lieu, Z. Z., Wolfenson, H., Hameed, F. M., Bershadsky A. D., & Sheetz, M. P. Mechanosensing Controlled Directly by Tyrosine Kinases. Nano Lett. **16**, 5951–5961 (2016).
[35] Bao G, Suresh S (2003) Cell and molecular mechanics of biological materials. *Nat Mater* 2(11):715-725.
[36] D. Donahue, OOMMF User's Guide, Version 1.0.Interagency Report NISTIR, 6376, 3 (2004).

[37] Landau, L., & Lifshitz, E. Electrodynamics of Continuous Media, Pergamon Press, (1960).
[38] Ghibaudo, M., Saez, A., et al. Tranction forces and rigidity sensing regulate cell functions. *Soft Matter* 4, 1836-1843 (2008).
[39] Guenat, O. T., & Berthiaume, F. (2018). Incorporating mechanical strain in organs-on-a-chip: Lung and skin. *Biomicrofluidics*, *12*(4), 042207
[40] Belmont, A.S., F.M. Kendall, & C.A. Nicolini. Coupling of nuclear morphometry to cell geometry and growth in human fibroblasts. Cell Biophys. **2**, 165-75 (1980).
[41] Li, Q., et al., The regulation of dynamic mechanical coupling between actin cytoskeleton and nucleus by matrix geometry. Biomaterials. **35**, 3, 961-9 (2014).
[42] Lovett, D.B., Shekhar, N., Nickerson, J.A., Roux, K.J. & Lele, T.P. Modulation of Nuclear Shape by Substrate Rigidity. Cell Mol Bioeng. **6**, 2, 230-238 (2013).
[43] Vishavkarma, R. et al. Role of Actin Filaments in Correlating Nuclear Shape and Cell Spreading. PLoS One. **9**, 9, e107895 (2014).
[44] Lodish, H. et al. Molecular Cell Biology. 4th edition, New York: W. H. Freeman (2000).
[45] Vartiainen, M.K., Guettler, S., Larijani, B. & Treisman, R. Nuclear actin regulates dynamic subcellular localization and activity of the SRF cofactor MAL. Science. **316**, 1749–1752 (2007).
[46] Miralles, F., Posern, G., Zaromytidou, A. I. & Treisman, R. Actin dynamics control SRF activity by regulationof its coactivator MAL. Cell. **113**, 3, 329-342 (2003).